

# From drag-reducing riblets to drag-increasing ridges

Lars H. von Deyn<sup>1,†</sup>, Davide Gatti<sup>1</sup> and Bettina Frohnafel<sup>1</sup>

<sup>1</sup>Institute of Fluid Mechanics, Karlsruhe Institute of Technology, Kaiserstr. 10, 76131 Karlsruhe, Germany

(Received 12 February 2022; revised 22 June 2022; accepted 2 September 2022)

Small drag-reducing riblets and larger drag-increasing ridges are longitudinally invariant and laterally periodic surface structures that differ only in the details of their lateral periodicity and their size in viscous units. Due to their different drag behaviour, typically riblets and ridges have been analysed separately. By studying experimentally trapezoidal-grooved surfaces of different sizes, we address systematically the transition from riblet-like to ridge-like behaviour in a unified framework. The structure height and lateral wavelength are varied both physically, by considering eight different surfaces, and in their viscous-scaled form, by spanning a wide range of bulk Reynolds number  $Re_b$ . The effective skin-friction coefficient  $C_f$  is determined via pressure-drop measurement in a turbulent channel flow facility designed for accurate drag measurements. An unexpectedly rich drag behaviour is unveiled, in which different drag regimes are distinguished depending on the value of  $l_g^+$ , the viscous-scaled square root of the groove area. The well-known drag-reducing regime of riblets that spans up to  $l_g^+ = 17$  is followed by a regime in which the roughness function  $\Delta U^+$  increases logarithmically with  $l_g^+$ , indicating an apparent fully rough behaviour up to  $l_g^+ \approx 40$ . Further increase of  $l_g^+$  leads to a clear departure from the fully rough regime, and an unexpected non-monotonic behaviour of the roughness function  $\Delta U^+$  for  $50 < l_g^+ < 200$  is reported for the first time. For sufficiently large  $Re_b$  and  $l_g$ , it is shown that a single parameter, similar to the classical hydraulic diameter, is sufficient to describe the drag behaviour of ridges. We find that an appropriate definition of the effective channel height is crucial for interpreting the drag behaviour. When the longitudinal protrusion height of the structured surface is accounted for in the channel height definition, a laminar flow exhibits the same  $C_f(Re_b)$  relation known for flat surfaces. This approach thus allows us to discern the modification of  $C_f$  induced by turbulence. We provide predictive correlations for the fully rough regime and the high

† Email address for correspondence: [von-deyn@kit.edu](mailto:von-deyn@kit.edu)

Reynolds number range of trapezoidal-grooved surfaces that become possible thanks to the chosen channel height definition.

**Key words:** turbulent boundary layers

## 1. Introduction

Two-dimensional (2-D) surface structures aligned with the main flow direction and periodically repeating with wavelength  $s$  in the direction perpendicular to it have been studied extensively over the last decades due to their capability to alter momentum and heat transfer properties of turbulent flows. Beside the details of the surface geometry, their height  $h$  and spacing  $s$  relative to the viscous length scale  $\nu/u_\tau$  determines the effect that such surfaces have on skin-friction drag (Goldstein & Tuan 1998; García-Mayoral, Gómez-De-Segura & Fairhall 2019). Here,  $\nu$  is the kinematic viscosity of the fluid, and  $u_\tau = \sqrt{\tau_w/\rho}$  is the friction velocity based on the average wall-shear stress  $\tau_w$  and fluid density  $\rho$ . Non-dimensionalization with viscous quantities is denoted with the superscript ‘+’ throughout the paper.

Small riblets are surfaces that, when spaced at wavelength  $s^+ \approx 15$ , are known to reduce skin-friction drag up to 10% in canonical flows at low values of the Reynolds number (Bechert *et al.* 1997). Various riblet shapes have been tested (Walsh & Lindemann 1984), and trapezoidal-grooved riblets, which yield 8.2% maximum drag reduction in similar conditions, are deemed a good compromise between drag-reducing performance, feasible manufacturing and durability (Bechert *et al.* 1997).

On the other hand, significantly larger streamwise invariant surface structures exceeding 100 viscous units in size typically yield the opposite effect and increase skin-friction drag. These drag-increasing structures, named ridges, are the object of many recent studies (see, for instance, Hwang & Lee 2018; Medjnoun, Vanderwel & Ganapathisubramani 2020; Stroh *et al.* 2020), where they are employed as a simplified model for laterally inhomogeneous roughness. Such roughness configurations are observed in a variety of natural and industrial turbulent flows, such as river bed flows (Colombini 1993) or flows over ablated turbine blades (Barros & Christensen 2014). Incorporating lateral inhomogeneities in roughness predictions remains an unsolved challenge (Chung *et al.* 2021), and simplified 2-D structures can serve as means to address explicitly the effect of spanwise inhomogeneities on skin-friction drag.

Despite the geometrical similarity of riblets and ridges, their skin-friction drag characteristics have not been related so far. Given the similarity, it is conceivable that observations and predictions made for riblets might extend to ridges, and vice versa, and thus the question arises of whether a unifying framework can be found to describe the drag properties of both surfaces. For the sake of clarity, since we will frequently resort to the terms riblets and ridges in the paper, it is worth discussing how structures are classified as belonging to either category in the following. Generally speaking, a 2-D surface is termed a riblet if it can potentially yield drag reduction, a capability that depends on the specific operating range and dimensions of the experimental facility. However, it is known (see, for instance, Endrikat *et al.* 2021) that typical riblet geometries such as the presently investigated trapezoidal grooves achieve drag reduction when the viscous-scaled square root of the groove area  $l_g^+$  (García-Mayoral & Jiménez 2011a), i.e. the fluid area between two consecutive riblet crests, is  $l_g^+ < 17$  (see also figure 1a). Moreover, riblets

From drag-reducing riblets to drag-increasing ridges

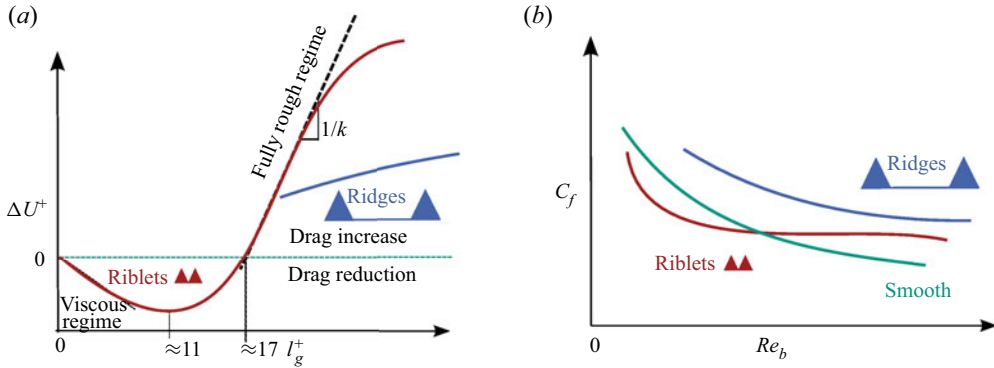


Figure 1. Schematic of different drag regimes. Hypothetical curves inspired by Gatti *et al.* (2020) for riblets and by Medjnoun *et al.* (2020) for ridges.

reduce drag only in turbulent flows (Bechert *et al.* 1997) such that the lower bound of the viscous-scaled half-channel height  $\delta^+$  (i.e. the friction Reynolds number) has to be beyond  $\delta^+ \approx 100$ . Thus only 2-D structures that fulfil

$$\frac{l_g}{\delta} \lesssim 0.17 \tag{1.1}$$

can potentially lead to drag reduction. Such structures are referred to as riblets throughout the present paper. In this paper, we will assess the drag behaviour of both surfaces characterized by  $l_g/\delta < 0.17$  (riblets) and surfaces that exceed  $l_g/\delta > 0.17$  (ridges).

Currently, only the skin-friction drag of small 2-D riblets is predictable from the geometrical properties of the surface alone. In the so-called viscous or linear regime of riblets, the flow in the riblet vicinity is dominated by viscosity and thus its behaviour can be described via Stokes flow solutions. Luchini, Manzo & Pozzi (1991) characterized the flow above riblets with streamwise and spanwise protrusion heights  $h_{\parallel}$  and  $h_{\perp}$ , respectively. The protrusion height is measured as the distance below the riblet tips at which the spatially averaged velocity profile obtained from the Stokes solution above the riblet tips predicts a zero velocity when extrapolated towards the wall. In this context,  $h_{\parallel}$  is associated with the streamwise flow, and  $h_{\perp}$  accounts for the virtual origin perceived by the predominant turbulence effect in the wall vicinity, i.e. the spanwise velocity fluctuations. If  $h_{\perp}$  is located closer to the riblet crest than  $h_{\parallel}$  – i.e. the virtual origin perceived by turbulent eddies is displaced further into the flow than the one perceived by the mean flow – then the skin-friction drag is reduced. Quantitatively,  $\Delta U^+ = -(h_{\parallel}^+ - h_{\perp}^+)$  holds for riblet sizes of the order of the viscous sublayer of the turbulent flow (Luchini *et al.* 1991). Here,  $\Delta U^+$  corresponds to the roughness function (Perry, Schofield & Joubert 1969), i.e. the downward shift of the mean streamwise velocity in the logarithmic layer. Negative values of  $\Delta U^+$  indicate drag reduction. Grüneberger & Hage (2011) confirmed experimentally the drag behaviour suggested for very small riblets based on the protrusion height difference  $h_{\parallel}^+ - h_{\perp}^+$ , which corresponds to a linear relation between drag reduction and  $l_g^+$ . This behaviour is referred to as the viscous regime, which breaks down once the riblet size substantially exceeds the viscous sublayer.

While the protrusion height difference captures the amount of achievable drag reduction,  $l_g^+$  has been shown to be an appropriate choice of length scale to describe the collapse of the drag reducing regime for different riblet types (García-Mayoral & Jiménez 2011a).

Ridges are known to induce drag increase (Medjnoun *et al.* 2020). This drag increase can be quantified through the roughness function  $\Delta U^+$  if the mean velocity profile exhibits a logarithmic law of the wall similar to smooth wall turbulence. The downward shift of the logarithmic region of the rough wall velocity profile compared to the smooth wall one is given by  $\Delta U^+$  (Chung *et al.* 2021). For rough surfaces (in particular so-called  $k$ -type roughness; Jiménez 2004),  $\Delta U^+$  increases linearly (slope  $1/\kappa$ ) with the logarithm of the viscous-scaled roughness size in the fully rough regime.

The typical drag behaviour of 2-D surfaces is sketched in figure 1, where figure 1(a) shows  $\Delta U^+$  as a function of  $l_g^+$ . As noted before, negative  $\Delta U^+$  indicates drag reduction. Concerning riblets, we observe the linear viscous region, after which the breakdown of the viscous regime begins with the maximum drag reduction reached at  $l_g^+ \approx 11$  (García-Mayoral & Jiménez 2011a). A further increase of  $l_g^+$  leads to an increasing friction with  $\Delta U^+ = 0$  at  $l_g^+ \approx 17$ . The occurrence of secondary flows consisting of matched pairs of streamwise vortices (Goldstein & Tuan 1998), or alternatively the emergence of Kelvin–Helmholtz (KH) instabilities, were proposed (García-Mayoral & Jiménez 2011b) as the mechanisms underlying the drag increase of riblets. Recent studies exploiting direct numerical simulations (DNS) in minimal channels indicate that KH instabilities contribute to an increase of  $\Delta U^+$ , but are not solely responsible for the breakdown of the viscous drag-reduction regime of riblets (Endrikat *et al.* 2021). In fact, only sharp-triangular and blade riblets show a significant friction contribution of KH rollers (Endrikat *et al.* 2021), whereas the breakdown of the viscous regime occurs inevitably for all riblets. Furthermore, Modesti *et al.* (2021) showed that secondary flows contribute significantly to  $\Delta U^+$  for various riblet shapes by analysing the dispersive stresses as a footprint of secondary flows.

As the mechanism associated with the viscous breakdown of riblets remains an open question, also the friction behaviour of larger 2-D structures ( $l_g^+ > 20$ ) is currently not well understood, whether they be riblets beyond the drag-reducing regime or ridges. When transitioning from the drag-reducing to the drag-increasing regime, Jiménez (2004) suggested that riblets might behave as regular ( $k$ -type) roughness. Global friction measurements reported by Gatti *et al.* (2020) confirm the initial agreement in the drag-increasing regime of riblets with the fully rough reference, but indicate a departure from the fully rough behaviour for  $l_g^+ > 40$ , as shown schematically in figure 1(a). Typically, in the fully rough state,  $\Delta U^+$  obeys the log-law  $\Delta U^+ = 1/\kappa \ln k^+ + B$ , where  $k$  is an appropriate roughness length scale,  $\kappa$  is the von Kármán constant, and  $B$  is a variable additive constant (Perry *et al.* 1969). Even for the relatively simple 2-D structures, the choice of roughness length scale is not obvious. Gatti *et al.* (2020) employed the structure height for one single set of drag-increasing riblets. Since the breakdown of the viscous regime collapses for different riblet geometries when scaled by  $l_g^+$  (García-Mayoral & Jiménez 2011a),  $l_g^+$  seems a sound choice for a roughness length scale between various riblet shapes.

The skin-friction coefficient  $C_f = 2\tau_w/(\rho U_b^2)$  is an alternative measure to assess fully rough behaviour, since its value becomes independent of the bulk Reynolds number  $Re_b = 2U_b\delta/\nu$  in the fully rough regime. In the case of channel flow,  $\delta$  denotes the half-channel height, and  $U_b$  is the bulk velocity. Schematically,  $C_f(Re_b)$  is sketched in figure 1(b) for trapezoidal-grooved riblets such as those assessed experimentally by Gatti *et al.* (2020) with respect to a smooth reference. For sufficiently small  $Re_b$ ,  $C_f$  is located below the value of the reference smooth wall, indicating drag reduction. A region of approximately

constant  $C_f(Re_b)$  follows at intermediate values of  $Re_b$ . Eventually,  $C_f$  begins to decrease again for sufficiently large  $Re_b$  (Gatti *et al.* 2020).

While the drag behaviour of riblets can be described *a priori* at least in the viscous regime, no such geometry-based description of ridge-induced drag has been developed so far. Recently, ridge-type 2-D structures have been investigated systematically by Medjnoun *et al.* (2020), who considered skin-friction drag and its interplay with secondary currents for triangular, rectangular and half-sphere shapes of the order of  $l_g^+ \approx 200$ . Based on oil-interferometry  $C_f$  measurements, they report a decreasing skin-friction coefficient  $C_f$  with increasing Reynolds number, indicating the absence of a fully rough regime for large 2-D structures, in agreement with channel flow pressure-drop measurements by von Deyn *et al.* (2019, 2021). The  $C_f$  versus  $Re_b$  behaviour of ridges is included schematically in figure 1.

Considering the friction behaviour of 2-D structures as sketched schematically in figure 1, the question arises of how and whether the drag behaviours of riblets and ridges differ or not. Therefore, we need to understand whether the drag-increasing behaviour of riblets as reported by Gatti *et al.* (2020) can be reproduced with other riblet shapes and sizes, and whether riblets at very large  $l_g^+$  eventually behave like ridges.

In order to tackle these questions, we analyse the global friction of 2-D trapezoidal-grooved structures and provide unprecedented friction measurements over a wide range of dimensionless structure size. By varying systematically height  $h$  and spanwise spacing  $s$  over one order of magnitude for a total of eight surface structures, measured individually in a bulk Reynolds number range  $4.5 \times 10^3 < Re_b < 8.5 \times 10^4$ , we are capable of varying  $l_g^+$  in the range  $1 < l_g^+ < 1340$ . We specifically chose the physical structure size of the riblet cases where  $l_g^+$  becomes sufficiently large to compare to ridge-type behaviour known from literature cases (e.g. Medjnoun *et al.* 2020). Vice versa, the  $l_g^+$  of ridge cases is designed to overlap with drag-increasing riblets. In doing this, we provide novel experimental evidence in a concerted study of riblets and ridges on different drag regimes and their connection, and discuss predictive options.

## 2. Turbulent drag definition and its implications

The definition of skin friction, Reynolds number and their relationship with the streamwise pressure gradient is straightforward for plane turbulent channel flows, but less so for parallel flows with complex cross-section, like the 2-D structures addressed in the present work. It is therefore discussed in the following.

Let the three velocity components be denoted  $(u_1, u_2, u_3) = (u, v, w)$  along the streamwise, wall-normal and spanwise  $(x_1, x_2, x_3) = (x, y, z)$  direction, respectively. For fully developed plane turbulent channel flow, the wall-shear stress  $\tau_w$  is a function of the time-averaged streamwise pressure gradient

$$\tau_w = -\frac{\partial \bar{p}}{\partial x_1} \delta, \quad (2.1)$$

where  $\delta$  corresponds to the half-channel height (see below) and  $\overline{(\cdot)}$  denotes time averaging. This relation is used in the present experimental campaign (see § 3) to obtain the skin-friction coefficient

$$C_f = \frac{2\tau_w}{\rho U_b^2}, \quad (2.2)$$

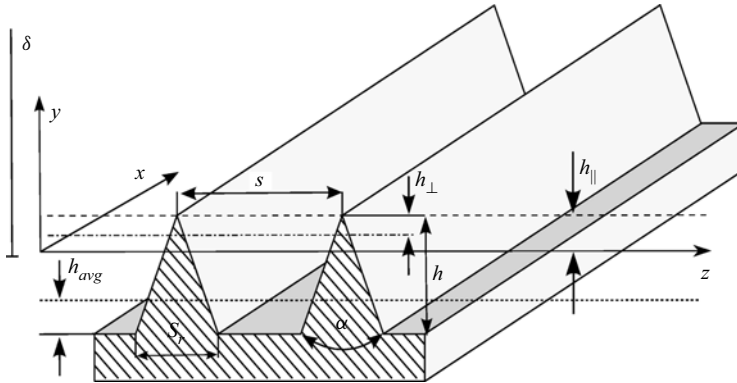


Figure 2. Sketch of investigated surface structures, where  $h_{||}$  and  $h_{\perp}$  represent streamwise and spanwise protrusion heights (Luchini *et al.* 1991), and  $h_{avg}$  is the averaged (melted-down) height. The half-channel height  $\delta$  is defined as the distance between the channel centreline and  $h_{||}$  below the structure tip.

where  $U_b$  is the bulk velocity (volume flow rate per unit width  $\dot{V}'$ , normalized by channel height  $2\delta$ ) also used for the formulation of the bulk Reynolds number

$$Re_b = \frac{2\delta U_b}{\nu} = \frac{\dot{V}'}{\nu}. \quad (2.3)$$

Additionally, based on  $\tau_w$ , the friction velocity  $u_\tau = \sqrt{\tau_w/\rho}$  and the respective friction Reynolds number  $Re_\tau = u_\tau \delta/\nu$  are obtained.

Equation (2.1) is derived for turbulent channels with plane walls, for which  $\tau_w$  then represents the temporally and spatially averaged wall-shear stress, and  $\delta$  is the univocally defined half-channel height. When the same equation is applied to non-planar surfaces,  $\tau_w$  assumes the different meaning of an effective wall-shear stress, which balances the measured pressure gradient as if it were caused by a virtual flat wall placed at distance  $\delta$  from the channel centreline. The definition of  $\delta$  is therefore not trivial when the walls are not flat.

We choose to place the wall-normal origin of the channel at the streamwise protrusion height  $h_{||}$  below the structure's tip for the present study (see figure 2). This ensures that the surface structures do not induce any drag variation under laminar flow conditions, as discussed in the following. In § 5.2 and the Appendix we present the evaluated drag change for alternative channel height definitions.

In order to determine  $h_{||}$  and  $h_{\perp}$ , a Stokes flow problem given by

$$-\frac{1}{\rho} \frac{\partial p}{\partial x_i} + \nu \frac{\partial^2 u_i}{\partial x_j \partial x_j} = 0 \quad (2.4)$$

in conjunction with the conservation of mass is solved numerically. Shear flow aligned with the surface structure is considered to obtain  $h_{||}$ , whereas (2.4) is solved for shear flow perpendicular to the structure orientation to obtain  $h_{\perp}$ . The protrusion heights,  $h_{||}$  and  $h_{\perp}$  correspond to the distance below the structure tip at which the spatially averaged Stokes solution extrapolates to zero. In this configuration, (2.4) simplifies to the Laplace equation  $\nabla^2 u = 0$  for the parallel flow configuration, and analytical solutions can be found in the case of 2-D structures via conformal mapping (Bechert & Bartenwerfer 1989). The values stated in table 2 below for  $h_{||}$  and  $h_{\perp}$  are computed numerically via finite elements utilizing

the software FreeFem++ (Hecht 2012). The procedure was validated against the analytical solution and literature references (Luchini *et al.* 1991; Bechert *et al.* 1997). For the present surface structures,  $h_{\perp}$  is located closer to the structure tip compared to  $h_{\parallel}$ , as visualized in figure 2. The figure also includes the meltdown height  $h_{avg}$ , which is located closer to the bottom of the surface structure.

For the investigated 2-D surface structures, the laminar channel flow solution and the Stokes flow solution for  $h_{\parallel}$  coincide. Therefore, the channel height definition based on  $h_{\parallel}$ , as indicated in figure 2, provides a set-up in which the well-known  $C_f$ - $Re_b$  relation for laminar channel flow ( $C_f = 12/Re_b$ ) also applies for a channel with riblets. Thus, by choosing the current definition of  $\delta$ , we focus on the surface structure influence on turbulent drag, since the laminar drags of smooth and structured channel are identical by definition. This is in agreement with the drag-reduction prediction for the viscous regime as outlined briefly in § 1, which suggests zero drag change for vanishing viscous-scaled riblet size (Luchini *et al.* 1991).

Although the drag force of a specific surface for a given flow rate is unambiguous, as it can be e.g. measured with a force sensor, its dimensionless representation does depend on the length scales used for normalization. As can be seen from (2.1) and (3.2), the choice of  $\delta$  enters the definitions of  $\tau_w$  and  $C_f$  and, through  $\tau_w$ , also affects all friction-related quantities such as  $I_g^+$ . Note that  $Re_b$  is independent of the choice of  $\delta$  since it is determined directly by the volume flow rate.

### 3. Test facility

The channel flow is generated by a blower-type wind tunnel (Mehta & Bradshaw 1979). The schematic set-up of the facility is shown in figure 3. The flow is driven by a radial fan with a large operational range  $40\text{--}6000\text{ m}^3\text{ h}^{-1}$ , and progresses through a supply pipe into a large settling chamber. The air is blown towards the back wall of the settling chamber, which is opposite the nozzle directing into the actual test section, in order to ensure a homogeneous flow distribution. The air flows through five grids embedded in wooden frames and a honeycomb flow straightener on its way through the settling chamber towards the test section. The arrangement of the radial fan outside the settling chamber minimizes the blockage and decouples the vibrations generated by the radial fan. A nozzle of contraction ratio 6 : 1 connects the settling chamber with the rectangular duct test section. There are 21 pairs of pressure taps (diameter 0.3 mm) spaced at intervals of 200 mm located along the side walls of the test section in order to measure the streamwise pressure gradient. Changes in ambient conditions are accounted for by tracking the inlet and outlet temperatures via PT100 thermocouples with maximum error below 0.1 K, and the ambient pressure  $p_{amb}$  and humidity  $a_q$  using Adafruit BMP 388 and BME 280 sensors, respectively. The BMP sensor has absolute accuracy 0.5 hPa, while the BME sensor resolves  $a_q$  with error  $\pm 3\%$ .

On the suction side of the radial fan, an inlet pipe of diameter  $D$  is installed. A zigzag tripping is located at the pipe entrance  $32D$  upstream of an orifice flow meter of diameter  $d$  and diameter ratio  $\beta = d/D$ , across which the pressure drop  $\Delta p_o$  is measured and related to the orifice flow rate

$$\dot{V}_o = \frac{C}{\sqrt{1 - \beta^4}} \epsilon \frac{\pi}{4} d^2 \sqrt{\frac{2 \Delta p_o}{\rho_{in}}}. \quad (3.1)$$

The coefficients  $C$  and  $\epsilon$  are derived from empirical expressions (International Organization for Standardization 2003b), where  $C$  depends on the diameter ratio  $\beta$  and

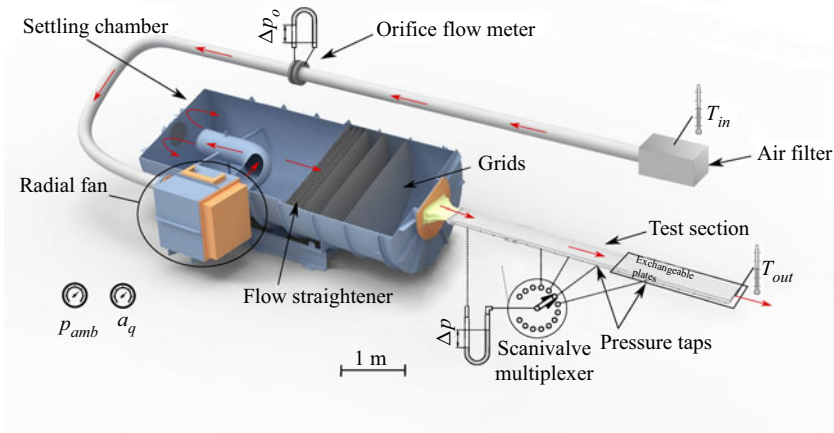


Figure 3. Schematic of the experimental facility with respect to wind tunnel components and measurement instrumentation.

| Marker      | Pipe diameter $D$ | Inner diameter $d$ | Approximate range in $Re_b$                |
|-------------|-------------------|--------------------|--|
| $\triangle$ | 100 mm            | 60 mm              | $4.5 \times 10^3 < Re_b < 1.3 \times 10^4$ |
| $\circ$     | 200 mm            | 105 mm             | $6 \times 10^3 < Re_b < 2.3 \times 10^4$   |
| $\diamond$  | 200 mm            | 120 mm             | $7 \times 10^3 < Re_b < 3.8 \times 10^4$   |
| $\square$   | 200 mm            | 150 mm             | $3 \times 10^4 < Re_b < 8.5 \times 10^4$   |

Table 1. Specifications of the different orifice flow meter configurations. Introduced markers are used in figures 4–10.

the pipe Reynolds number  $Re_D$  (Sattary & Reader-Harris 1996). As a result, the orifice flow rate  $\dot{V}_o$  is computed with the iterative procedure outlined in norm EN (International Organization for Standardization 2003a), since  $Re_D$  itself is dependent on  $\dot{V}_o$ . The mass flow rate  $\dot{m}$  through the pipe (and thus also the channel test section) is obtained based on multiplication of the volume flow rate with the air density  $\rho_{in}$  deduced from the ideal gas law including humidity effects and a temperature measurement  $T_{in}$  at the pipe inlet.

In order to keep the dissipative losses generated by the orifice flow meter within reasonable limits and to avoid compressibility effects, a maximum differential pressure  $\Delta p_{omax} = 625$  Pa across the orifice is considered, thereby limiting the maximum achievable flow rate for a given  $d$ . For the sake of covering a range of the bulk Reynolds number  $4.5 \times 10^3 < Re_b < 8.5 \times 10^4$  (this corresponds to  $150 \lesssim Re_\tau \lesssim 2000$  for the smooth wall case) in the test section, two different orifice flow meters are installed with inlet pipe diameters  $D = 100$  mm and  $D = 200$  mm, respectively. Each custom-manufactured annular orifice measuring chamber can be equipped with orifice plates of varying inner diameter  $d$ . The configurations are specified in table 1. The orifice's pressure drop is measured with one of two Setra 239D (125 Pa and 625 Pa full-scale) unidirectional differential pressure transducers with accuracy 0.07 % of the full scale, switching automatically depending on  $\Delta p_o$ .

The resulting (effective) wall-shear stress in the considered portion of the channel test section is determined by evaluating the streamwise pressure gradient at a given flow rate.

## From drag-reducing riblets to drag-increasing ridges

Based on the measured pressure gradient  $\Pi = -(\Delta\bar{p}/\Delta x)$  and the measured mass flow rate  $\dot{m} = \dot{V}_o\rho_{in}$ , the skin-friction coefficient is computed via

$$C_f = \frac{8\Pi\delta^3W^2\rho}{\dot{m}^2}, \quad (3.2)$$

where  $\rho$  denotes the density at the test section's outlet, and  $W$  is the test section width. For the pressure measurement, an MKS Baratron 698A unidirectional differential pressure transducer with 1333 Pa maximum range and accuracy 0.13 % of the reading is employed. In order to measure the pressure drop at all streamwise pressure taps, a Scanivalve multiplexer is used that switches mechanically between the individual pressure taps such that all pressure differences are measured with the same high-accuracy pressure transducer.

The test section consists of a flat rectangular duct of aspect ratio  $AR = 12$ , with  $W = 0300$  mm and  $\delta = 12.6$  mm in the smooth reference case. It extends in the streamwise direction  $L = 3950$  mm, corresponding to  $L = 313.5\delta$ . Two plates for the top and bottom walls, as well as two monolithic rods for the side walls, form the test section. The duct walls are made of polished aluminium of average roughness  $Ra = 0.4$  mm, and the top and bottom walls consist of three segments (950 mm, 1500 mm, 1500 mm) that can be exchanged individually.

The bulk Reynolds number in the test section is constant along its length and computed via

$$Re_b = \frac{\dot{m}}{W\rho v}. \quad (3.3)$$

Two trip strips are installed at the inlet of the test section along the whole channel width. Each strip protrudes 1.6 mm ( $0.13\delta$ ) from the wall and extends for 0.3 mm in the streamwise direction, resulting in 13 % cross-section blockage. The trip provides fully-developed turbulent flow conditions for  $Re_b > 4500$  starting  $160\delta$  downstream of the tripping location (Güttler 2015).

The measurement uncertainty is quantified via Gaussian error propagation at 95 % confidence level, as outlined in the Appendix of Gatti *et al.* (2015) for the utilized facility. The accumulated uncertainty of  $C_f$  is below  $\pm 2.7$  %, where the biggest uncertainty contribution stems from the orifice flow rate measurement with  $\pm 1.7$  %. Assuming the error in the flow rate measurement to be systematic, and considering only the error arising from the measurement instrumentation (i.e. random error sources), the measurement uncertainty for drag change measurements  $\Delta C_f/C_{f0}$  (where  $C_{f0}$  denotes the smooth reference value at matched  $Re_b$ ) reduces to 0.4 % (Güttler 2015).

### 4. Experimental matrix

For the present investigation, 8 sets of 2-D trapezoidal-grooved geometries of varying height  $h$  and spacing  $s$  are considered (see figure 2 for geometrical definitions), which are installed on both channel walls symmetrically in the most downstream  $119\delta$  of the test section. All cases are listed in table 2. The naming convention is introduced following the distinction between riblets and ridges outlined in the Introduction: an ID starting with dr refers to potentially drag-reducing riblets with  $l_g/\delta < 0.17$ , and purely drag-increasing ridges that exceed  $l_g/\delta > 0.17$  are labelled di.

The number part of the ID represents the ratio of the wavelength  $s$  and the structure width  $s_r$ , i.e. dr\_1a, ..., dr\_1c are sawtooth riblets, while di\_13 are widely spaced ridges.

| ID    | $s/\delta$ | $h/\delta$ | $s/s_r$ | $\alpha$<br>(deg.) | $l_g/\delta$ | $l_g/s$ | $P/s$ | $h_{\parallel}/s$<br>( $\times 10^{-1}$ ) | $h_{\perp}/s$<br>( $\times 10^{-2}$ ) | $\eta_c$ |
|-------|------------|------------|---------|--------------------|--------------|---------|-------|---|---------------------------------------|----------|
| dr_1a | 0.0068     | 0.0072     | 1       | 51.1               | 0.0049       | 0.709   | 2.31  | 1.791                                     | 8.083                                 | —        |
| dr_1b | 0.0136     | 0.0144     | 1       | 50.6               | 0.0099       | 0.729   | 2.34  | 1.795                                     | 8.089                                 | —        |
| dr_1c | 0.0808     | 0.0703     | 1       | 60                 | 0.0533       | 0.660   | 2.01  | 1.707                                     | 8.017                                 | —        |
| dr_2  | 0.0492     | 0.0235     | 2.07    | 53.5               | 0.0302       | 0.614   | 1.59  | 1.744                                     | 8.021                                 | —        |
| di_2  | 0.4423     | 0.1666     | 2.3     | 60                 | 0.2401       | 0.543   | 1.44  | 1.643                                     | 7.946                                 | 0.933    |
| di_4  | 0.7569     | 0.1639     | 4       | 60                 | 0.3295       | 0.435   | 1.25  | 1.359                                     | 7.865                                 | 0.956    |
| di_8  | 1.4909     | 0.1614     | 8       | 60                 | 0.4749       | 0.319   | 1.13  | 0.869                                     | 6.538                                 | 0.97     |
| di_13 | 2.1572     | 0.158      | 13.2    | 54.8               | 0.5726       | 0.265   | 1.09  | 0.635                                     | 5.23                                  | 0.974    |

Table 2. Dimensions of the investigated geometries as introduced in figure 2. Here,  $P$  denotes the perimeter,  $l_g$  is the square root of the groove area as introduced by García-Mayoral & Jiménez (2011a),  $h_{\parallel}$ ,  $h_{\perp}$  are the streamwise and spanwise protrusion heights measured from the tip as defined by Luchini *et al.* (1991), and  $\eta_c$  represents a constant hydraulic channel height relation  $\delta_{hyd}/\delta = \text{const.}$  (see (5.6) for the definition of  $\delta_{hyd}$ ) obtained *a posteriori* from figure 10.

Both  $h$  and  $s$  are varied systematically over one order of magnitude. For the interested reader, note that the mean flow data of di\_13 up to  $Re_b = 5 \times 10^4$  is discussed in von Deyn *et al.* (2021). Moreover, set dr\_2 corresponds to the one discussed in Gatti *et al.* (2020).

In doing this, the evolution of the drag change with respect to a smooth surface is studied starting from very small drag-reducing riblets submerged in the viscous sublayer up to widely spaced drag-increasing ridges that protrude into the logarithmic flow region and are known to induce large-scale secondary motions (Medjnoun *et al.* 2020). Note that di\_2 was designed purposely as an enlarged trapezoidal riblet geometry. To quantify the increase in wetted surface area, the perimeter  $P$  to spanwise wavelength ratio  $P/s$  is included in table 2. For each geometry, the Stokes flow solution (see § 2) is computed to obtain the protrusion height values  $h_{\parallel}$  and  $h_{\perp}$ .

The changes in skin-friction drag  $\Delta C_f$  are obtained by comparing two consecutive experiments: first, a smooth wall measurement used as a common reference for all structured cases was conducted, followed by skin-friction measurements of the structured plates. The smooth data are fitted with a polynomial function of fifth order for each orifice configuration stated in table 1, enabling a comparison at constant flow rate between smooth and structured cases. All measurements are carried out in the most downstream third 1500 mm (or  $119\delta$ ) portion of the test section, allowing  $194\delta$  for flow development. The pressure taps in the second segment are used as a reference to confirm reproducibility between different measurements. The investigated structures were milled in 1500 mm-long aluminium plates with a high precision CNC milling-machine, with the exception of sets dr\_1a and dr\_1b, which consist of a riblet foil manufactured by 3M glued onto aluminium plates. The net half-channel height  $\tilde{\delta}_{avg}$ , defined as the distance between the channel centreline and the average structure height  $h_{avg}$  (see figure 2), is adjusted to match the smooth reference value  $\delta = 12.6$  mm. In doing so, the net fluid volume in the channel is kept identical between different cases. This set-up was chosen initially because we considered  $\tilde{\delta}_{avg}$  an appropriate channel height for the comparison among different types of riblets and ridges. As will be discussed in § 5.2, a more physically sound choice for interpreting the measurements is  $\delta$  based on  $h_{\parallel}$ . Thanks to the use of dimensionless numbers, the choice of channel height in the experimental set-up can be converted easily to other choices in the data evaluation.

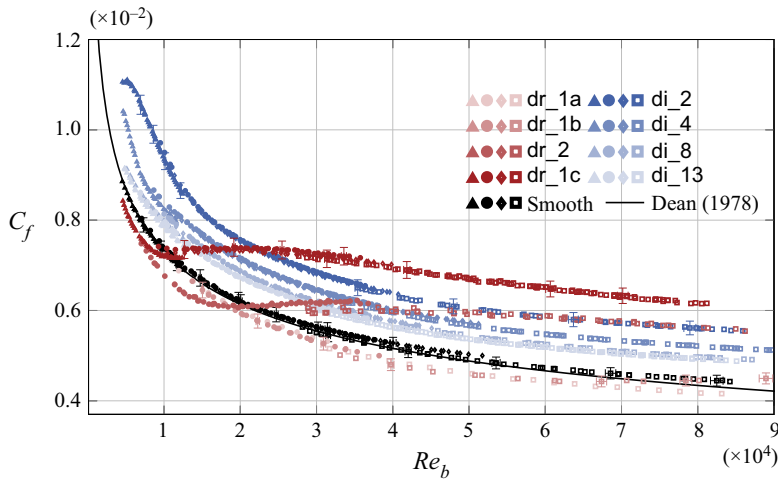


Figure 4. Skin-friction coefficient  $C_f$  as a function of the bulk Reynolds number  $Re_b$ . Different markers indicate different orifice diameters as introduced in table 1. Riblets (dr, drag-reducing) are depicted in red, and ridges (di, purely drag increasing) are shown in blue. The reference measurements (black markers) are shown in comparison to the correlation proposed by Dean (1978). The horizontal and vertical error bars represent the measurement uncertainty for exemplary data points.

The geometrical parameters stated in table 2 were verified via optical (Sensofar S neox) and tactile measurements (perthometer Mahr MarSurf PCV). Next to the geometrical parameters  $s$ ,  $h$ ,  $s_r$  and  $\alpha$  as defined in figure 2, the square root of the groove area  $l_g$  and the perimeter  $P$  are included in table 2.

## 5. Measurement results

In order to assess the skin-friction drag and identify respective drag regimes, the pressure-drop measurement results obtained for all surface structures specified in table 2 and the smooth reference are analysed in the following.

### 5.1. Skin-friction measurements

The skin-friction coefficient  $C_f$  (see (2.2)) as a function of  $Re_b$  is presented in figure 4. The smooth results are shown as black markers with respect to the well-known correlation proposed by Dean (1978). The different markers denote the varying orifice flow meter sizes employed to measure the volumetric flow rate (see § 3). Overall, the reference results show very good agreement with the Dean correlation with detected deviations below 2.7%, i.e. within the measurement uncertainty margin. Also note that the data collected by Dean (1978) to derive his famous correlation are subject to significant scatter.

The colour code is introduced following the distinction between riblets and ridges: riblet data are depicted with red symbols in different shades, while ridge data are shown in shades of blue. Lighter colours indicate physically smaller riblets, or more widely spaced ridges. Sets dr\_1a, dr\_1b, dr\_1c and dr\_2 are at least partially located below the smooth reference in the Nikuradse-type diagram of figure 4, indicating that these surfaces reduce skin-friction drag in this particular Reynolds number range in the present facility. The drag-reducing effect scales in viscous units (Bechert *et al.* 1997), thus the drag-reducing regime of the different structures is shifted to lower  $Re_b$  with increasing ID/colour intensity

(a,b,c and 2) due to their increasing physical size. All drag-increasing structures (in blue) reveal a monotonically decreasing  $C_f$  with increasing  $Re_b$ , indicating that none of the investigated geometries reaches an apparent fully rough (i.e.  $C_f$  independent of  $Re_b$ ) flow state in the investigated Reynolds number range.

The physically larger riblet sets dr\_1c ( $l_g/\delta = 0.0533$ ) and dr\_2 ( $l_g/\delta = 0.0302$ ) are one order of magnitude larger than the smallest riblet set dr\_1a ( $l_g/\delta = 0.0049$ ). They transition from a drag-reducing to a drag-increasing behaviour within the present Reynolds number range, exhibiting a region of constant  $C_f$  for a limited range of Reynolds numbers before eventually showing  $C_f(Re_b)$  behaviour similar to that of the drag-increasing ridges. A trace of nearly constant  $C_f$  is also present for di\_2 ( $l_g/\delta = 0.2401$ ) at very low Reynolds numbers, which hints at a similarity between the two surface structures di\_2 and dr\_2.

The measurement results of the differently spaced ridge configurations reveal that narrower-spaced ridges (darker blue colour) of the same element height produce more skin-friction drag compared to wider-spaced ridges, i.e. skin-friction drag increases with increasing perimeter  $P$  to wavelength  $s$  ratio  $P/s$ . However, we observe that the increase in  $C_f$  is not simply proportional to the ratio  $P/s$ . A further discussion of this geometrical parameter is presented in § 5.3.4.

Locally, e.g. for set dr\_1c at  $Re_b \approx 3 \times 10^4$ , small (<2%) differences of  $C_f$  between the different orifice flow meter configurations can be observed. As specified in table 1, the different orifice configurations are necessary to cover the full range of  $Re_b$ . The observed scatter in the data points is related to systematic uncertainty arising from the flow rate measurement, and is within the expected measurement uncertainty discussed in § 3. Also note that the flow rate uncertainty is a function of the orifice pressure drop  $\Delta p_o$ , increasing nonlinearly for small  $\Delta p_o$ . Therefore, the overlap of  $C_f$  measurements obtained with different orifices is particularly challenging, since one of them must work towards its lower  $Re_b$  limit of applicability, as specified in table 1, i.e. at low  $\Delta p_o$  and larger uncertainty. However, the offset in  $C_f$  induced by the flow rate measurement is independent of the investigated individual surface structure. Therefore, the offset error cancels when evaluating the relative drag change  $(C_f - C_{f0})/C_{f0} = \Delta C_f/C_{f0}$  or  $\Delta U^+$  discussed in the following subsections. In consequence, the resulting uncertainty for these relative quantities is significantly smaller.

## 5.2. Implications of the channel height definition

As discussed in § 2, the arbitrary choice of the effective half-channel height directly affects  $C_f$  and many other flow quantities. In the present work, the wall-normal origin has been placed a streamwise protrusion height  $h_{\parallel}$  below the surface crest, which is the position where the far-wall Stokes flow oriented in the mean turbulent flow direction predicts zero average velocity. For non-planar surfaces, the resulting half-channel height  $\delta$  differs from the average half-channel height  $\tilde{\delta}_{avg}$ , which is defined as the distance between the average structure height  $h_{avg}$  (see figure 2) and the channel centreline. This definition is commonly used for rough surfaces due to its relatively easy accessibility (Chan *et al.* 2015).

In order to show that the present choice of the effective channel height is particularly suited to assess the effect of 2-D structures on turbulent drag, we compare how the relative drag change varies when it is computed assuming half-channel heights  $\delta$  and  $\tilde{\delta}_{avg}$ , respectively. For the sake of clarity, quantities computed with  $\tilde{\delta}_{avg}$  are denoted with  $(\tilde{\cdot})$ .

The corresponding results for  $\Delta C_f/C_{f0}$  are presented in figure 5 for the riblet data sets, where figure 5(a) shows  $\Delta \tilde{C}_f/\tilde{C}_{f0}$ . Utilizing  $\tilde{\delta}_{avg}$  as half-channel height, i.e. placing the

From drag-reducing riblets to drag-increasing ridges

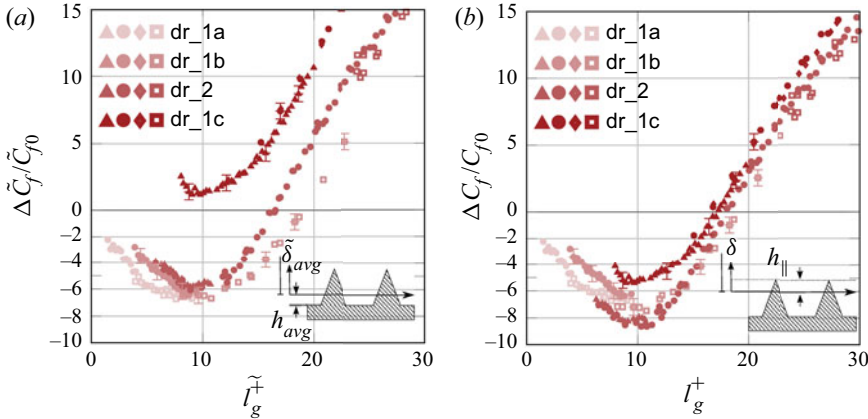


Figure 5. Relative drag change  $\Delta C_f/C_{f0}$  versus the viscous-scaled square root of the groove cross-sectional area  $l_g^+$ , with zoomed view on  $\Delta C_f/C_{f0} < 0$ . (a) Wall-normal origin placed at the averaged structure (meltdown) height  $h_{avg}$ , where  $\tilde{(\cdot)}$  is used to denote the change of the wall-normal origin to  $h_{avg}$  above the structure valley. (b) Wall-normal origin placed at  $h_{||}$  below the structure crest. The vertical error bars represent the measurement uncertainty for exemplary data points. The horizontal error bars are negligible in this representation.

wall-normal origin at the average (meltdown) height, corresponds to comparing  $\tilde{C}_f$  of the structured surface against  $\tilde{C}_{f0}$  of a reference channel with the same cross sectional area and at the same  $Re_b$ . The physically small ( $h < 0.3$  mm, i.e.  $h/\delta < 0.0235$ ) riblet sets dr\_1a, dr\_1b and dr\_2 show the expected negative  $\Delta\tilde{C}_f/\tilde{C}_{f0}$ , in agreement with previous wall-shear stress balance results of Bechert *et al.* (1997). Compared at the same viscous-scaled riblet size, one would expect the geometrically similar but physically larger data set dr\_1c ( $h/\delta = 0.0703$ ) to behave similarly to dr\_1a and dr\_1b. However, this is clearly not the case, as shown in figure 5(a), where  $\Delta\tilde{C}_f/\tilde{C}_{f0}$  is generally positive for dr\_1c. Moreover, the zero crossing  $\Delta\tilde{C}_f/\tilde{C}_{f0} = 0$  for data sets dr\_1b and dr\_2 does not occur at  $l_g^+ \approx 17$ , as commonly reported for riblets (García-Mayoral *et al.* 2019; Endrikat *et al.* 2021). Therefore, even though  $\Delta\tilde{C}_f/\tilde{C}_{f0}$  is an easily accessible quantity and thus might seem favourable at first glance, considering the drag change at matched cross-sectional area and flow rate does not result in collapsing drag curves for different data sets, and yields evidence contrasting the present understanding of riblets from the literature.

As an alternative, figure 5(b) shows  $\Delta C_f/C_{f0}$ . Note that  $\delta$  is generally smaller than  $\tilde{\delta}_{avg}$  for structured surfaces. Thus utilizing  $\delta$  as half-channel height corresponds to comparing  $C_f$  of the structured surface against  $C_{f0}$  of a reference channel with a slightly larger cross-sectional area and at the same  $Re_b$ . The data presented in figure 5(b) can be related directly to the  $\tilde{\delta}_{avg}$ -based scaling via the expressions:

$$\frac{\Delta C_f}{C_{f0}} = \left( \frac{\Delta\tilde{C}_f}{C_{f0}} + 1 \right) \frac{\delta^3}{\tilde{\delta}_{avg}^3} - 1, \quad l_g^+ = \tilde{l}_g^+ \sqrt{\frac{\delta}{\tilde{\delta}_{avg}}}. \quad (5.1a,b)$$

In comparison to figure 5(a), the differences are largest for the physically large riblets. This is due to the fact that in the case of the physically smallest set, dr\_1a ( $h/\delta = 0.0072$ ),  $\delta$  is only 0.2% smaller compared to  $\tilde{\delta}_{avg}$ , while for dr\_1c ( $h/\delta = 0.0703$ ), the two heights differ by 2.2%. In figure 5(b), the expected  $\Delta C_f/C_{f0}$  behaviour is recovered. All riblet

data sets yield negative  $\Delta C_f/C_{f0}$  for small  $l_g^+$ , and a better data collapse around the zero crossing at  $l_g^+ \approx 17$  is obtained. This indicates that the  $h_{\parallel}$ -based definition of  $\delta$  is better suited to compare data sets of strongly varying physical size at the additional expense of evaluating the Stokes flow solution.

In the drag-reducing regime, sets dr\_1a, dr\_1b and dr\_2 exhibit the expected  $\Delta C_f/C_{f0}$  trends, while set dr\_1c yields 38 % less maximum  $\Delta C_f/C_{f0}$  compared to the geometrically similar sets dr\_1a and dr\_1b. This is a result of the challenging manufacturing process: instead of the desired sharp tips, set dr\_1c has rounded tips with 70 mm curvature radius, i.e.  $R/s = 0.07$ . In this respect, data set dr\_1c agrees well with the findings of Walsh (1990), who reported 40 % decrease of  $\Delta C_f/C_{f0}$  for tip radius to spanwise spacing ratio  $R/s = 0.08$ . Note that only the maximum  $\Delta C_f/C_{f0}$  is affected by the tip rounding, while the optimum  $\Delta C_f/C_{f0}$  still occurs at  $l_g^+ \approx 11$ , as discussed previously by García-Mayoral & Jiménez (2011a). It is noteworthy that sets dr\_1a and dr\_1b are expected to collapse due to their geometric similarity. The visible deviations and slightly smaller  $\Delta C_f/C_{f0}$  of dr\_1b can be an effect of local imperfections observable visually on the 3M riblet foils. The influence of further channel height definitions on the present data evaluation is shown in the Appendix.

### 5.3. Drag regimes

As introduced with the schematic in figure 1, the data evaluation in terms of roughness function  $\Delta U^+$  allows us to distinguish different drag regimes. Figure 6 shows  $\Delta U^+$  against  $l_g^+$  for all investigated cases. Here,  $\Delta U^+$  is retrieved from  $C_f$  and  $C_{f0}$  measured at the same  $Re_b$  via the relationship

$$\Delta U^+ = \frac{1}{\kappa} \ln \sqrt{\frac{C_f}{C_{f0}}} + \sqrt{\frac{2}{C_{f0}}} - \sqrt{\frac{2}{C_f}}, \quad (5.2)$$

which is obtained from the Prandtl–von Kármán friction relation as described in Gatti *et al.* (2020), i.e. by approximating the change  $\Delta U_c^+$  of centreline velocity, unknown for the present experiment, with the change  $\Delta U_b^+$  of bulk velocity. This methodology is also employed in other studies dealing with pressure-drop measurements of flows over irregular roughness (Barros, Schultz & Flack 2018; Flack, Schultz & Barros 2020). The viscous-scaled mean velocity profile retrieved from DNS data (see von Deyn *et al.* 2021), which is available for the case di\_13, hints at the applicability of the described framework also for large ridges.

#### 5.3.1. Drag-reducing regime

The viscous prediction introduced by Luchini *et al.* (1991) for the physically smallest riblet set dr\_1a is also included in figure 6 and can be expressed as

$$\Delta U^+ = \frac{h_{\parallel} - h_{\perp}}{l_g} l_g^+ = -0.14 l_g^+ \quad (5.3)$$

for the viscous regime (García-Mayoral *et al.* 2019). The measurement results show excellent agreement with this viscous prediction for  $1 < l_g^+ < 7$ , thus confirming its applicability as also demonstrated previously by Grüneberger & Hage (2011). As noted before, the smaller drag reduction achieved with the geometrically similar data set dr\_1b is probably related to local imperfections of this riblet foil. For increasing  $l_g^+$ ,  $\Delta U^+$  deviates

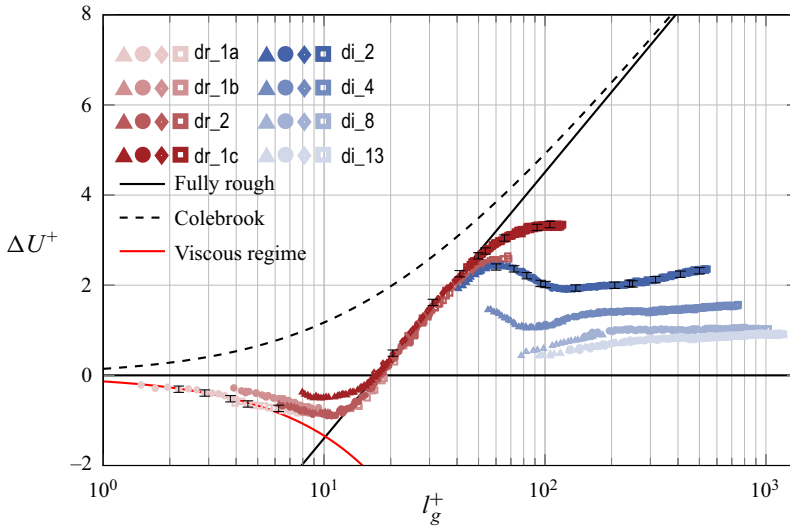


Figure 6. Roughness function  $\Delta U^+$  versus  $l_g^+$ . The black solid line represents the fully rough behaviour (see (5.4)) with  $\kappa = 0.39$  and  $B = -7.3$ . The red solid line represents the viscous friction prediction with  $\Delta U^+ = ((h_{\parallel} - h_{\perp})/l_g)l_g^+ = -0.14l_g^+$  computed for set dr\_1a. Additionally, the Colebrook roughness function is included for reference as a black dashed line (Colebrook *et al.* 1939). The vertical error bars represent the measurement uncertainty for exemplary data points. The horizontal error bars are negligible in this representation.

from the predicted behaviour and the well-known breakdown of the viscous regime occurs, leading to an increase of  $\Delta U^+$  past the point of maximum drag reduction. In agreement with literature data, the drag-reducing regime extends up to  $l_g^+ \approx 17$ , where  $\Delta U^+ = 0$  is found.

### 5.3.2. Fully rough drag regime

For even larger  $l_g^+$ , the fully rough drag regime follows. In this regime, the riblet surfaces, which cannot induce any pressure drag due to their streamwise invariant surface, reveal an apparent fully rough behaviour (typically attributed to the dominance of pressure drag on roughness elements). The data sets dr\_1b, dr\_1c and dr\_2 show remarkably good agreement. In addition, data set di\_2 – which is geometrically similar to dr\_2 – also reaches into this region and partially overlaps with dr\_2. We note that this collapse between riblets and ridges is obtained only for a data evaluation based on the half-channel height  $\delta$ . The alternative channel height definitions discussed in § 5.2 and in the Appendix do not yield this collapse. For reference, the Colebrook roughness function (Colebrook *et al.* 1939) is also included in figure 6, which does not capture the observed trends as it is also found for irregular roughness (Chung *et al.* 2021).

The good collapse of all experimental data indicates that the combination of  $l_g^+$  and a half-channel height definition based on  $h_{\parallel}$  are particularly well-suited for the description of the fully rough drag regime that extends up to  $l_g^+ \approx 40$ . Note that choosing  $s^+$  or  $h^+$  leads to worse agreement between data sets compared to  $l_g^+$ . The corresponding relation between  $\Delta U^+$  and  $l_g^+$  corresponds to the one of a classical fully rough surface (Perry *et al.* 1969)

with  $l_g^+$  as the roughness length scale

$$\Delta U^+(l_g^+) = \frac{1}{\kappa} \ln l_g^+ + B. \quad (5.4)$$

Employing a von Kármán constant  $\kappa = 0.39$  yields an additive constant  $B = -7.3$ . A comparison with the corresponding relation for the Nikuradse sand grain roughness  $\Delta U^+(k_s^+) = (1/\kappa) \ln k_s^+ - 3.5$  (Chung *et al.* 2021) results in an equivalent sand grain roughness

$$k_s^+ = l_g^+/4.4 \quad (5.5)$$

for the investigated surface structures. The equivalent sand grain roughness of the identified fully rough regime of riblets and ridges appears thus to be predictable based on the geometrical properties of the surface, in particular  $l_g$  and  $h_{\parallel}$ . This is a remarkable result since the identification of such links between surface topography and the hydraulic roughness scale  $k_s$  (and thus the related drag) is one of the key issues in roughness research due to large uncertainties in the existing predictive correlations (Chung *et al.* 2021). In analogy to (5.3), (5.5) or (5.4) can thus be employed directly to predict the drag of 2-D streamwise-aligned trapezoidal-grooved surface structures in a certain region of  $l_g^+$ , here  $17 \lesssim l_g^+ \lesssim 40$ .

### 5.3.3. Non-monotonic regime

Beyond  $l_g^+ \approx 40$ ,  $\Delta U^+$  exhibits a weaker increase with  $l_g^+$  than in the preceding fully rough drag regime. The present data sets confirm the deviation from the logarithmic increase of  $\Delta U^+$  around  $l_g^+ \approx 40$  reported previously by Gatti *et al.* (2020) (based on data set dr\_2) for additional riblet (data set dr\_1c) and ridge (data set di\_2) structures.

Then  $\Delta U^+$  increases mildly for  $200 < l_g^+ < 1000$ . Before this mild increase is reached, data sets di\_2 and di\_4 reveal a particular behaviour, most striking for di\_2, that is reported for the first time. Following the deviation from the fully rough regime,  $\Delta U^+$  reaches a local maximum at  $l_g^+ \approx 60$  before it decreases towards a local minimum at  $l_g^+ \approx 100$ –200. Set di\_4 also exhibits this non-monotonic behaviour in  $\Delta U^+$ , with a local minimum around  $l_g^+ \approx 85$ .

Based on these observations, an additional regime can be introduced where  $\Delta U^+$  decreases unexpectedly and which we term the non-monotonic regime. This regime can be identified in only two of the present data sets, and it remains to be investigated in future studies whether this non-monotonic behaviour of  $\Delta U^+$  featuring local maxima and minima is a universal feature of 2-D longitudinally aligned surface structures.

### 5.3.4. Hydraulic channel height regime

The observed mild increase of  $\Delta U^+$  for  $200 < l_g^+ < 1000$  for the ridge cases corresponds to a Reynolds number range in which the data sets di\_2, ..., di\_13 exhibit  $C_f$  curves that seem retrievable by shifting the  $C_{f0}$  versus  $Re_b$  curve upwards (see figure 4). In other words, the  $C_f$  curves of the structured surfaces could be derived by multiplying the smooth reference by a constant factor. Such a procedure is comparable to the common definition of the hydraulic diameter  $D_{hyd} = 4A/P$ , where  $A$  corresponds to the duct cross-section and  $P$  to the wetted perimeter (Schiller 1923). Pirozzoli (2018) showed that this classic definition is not applicable for ducts with high aspect ratios, and presented an alternative formulation for the hydraulic diameter. However, this formulation assumes a constant distribution of

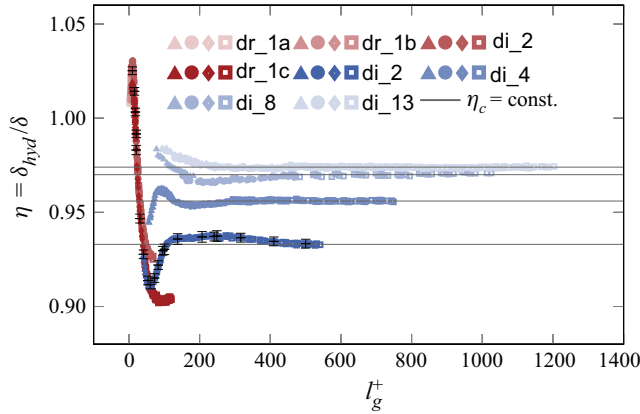


Figure 7. Hydraulic half-channel height ratio  $\eta = \delta_{hyd}/\delta$  obtained from (5.6) versus  $l_g^+$ . Grey lines indicate values for constant  $\eta$ , referred to as  $\eta_c$ . The corresponding values are included in table 2. The vertical error bars represent the measurement uncertainty for exemplary data points. The horizontal error bars are negligible in this representation.

wall-shear stress across the span, which is a fair assumption for ducts whose cross-section varies mildly and regularly, but clearly does not hold for the present trapezoidal-grooved surfaces.

In order to assess whether the present data can be described by a concept similar to a hydraulic diameter approach, we evaluate a hydraulic half-channel height  $\delta_{hyd}$  *a posteriori* for each surface structure and  $Re_b$ . If  $\delta_{hyd}$  assumes a constant value independently of  $Re_b$ , then the friction behaviour in this regime can be described solely by the ratio  $\delta_{hyd}/\delta$  and the smooth wall  $C_{f0}(Re_b)$  correlation, in analogy with the well-established hydraulic diameter concept for low-aspect-ratio ducts.

For each  $(C_f, Re_b)$  pair measured for a considered 2-D surface, we compute  $\delta_{hyd}$  by answering the question: ‘what would be the channel height of a smooth channel driven at the same flow rate that yielded the same skin-friction coefficient?’ Therefore,  $\delta_{hyd}$  is expressed based on the ratio  $C_{f0}/C_f$  via (3.2), such that

$$\delta_{hyd} = \delta \left( \frac{C_{f0}}{C_f} \right)^{1/3}. \quad (5.6)$$

In analogy to the definition of the smooth wall reference channel height  $\delta$  (based on an identical  $C_f(Re_b)$  correlation for smooth and structured walls under laminar flow conditions),  $\delta_{hyd}$  represents the channel height of a smooth wall reference channel with the same friction coefficient under turbulent flow conditions. The ratio  $\eta = \delta_{hyd}/\delta$  can thus be interpreted as a measure for the effective change in hydraulic channel height due to turbulence.

Figure 7 shows  $\eta$  as a function of  $l_g^+$ . Riblets that yield  $\Delta C_f/C_{f0} < 0$  (see figure 5) result in values  $\eta > 1$ , while the opposite occurs for  $l_g^+ > 17$  (where  $\Delta C_f/C_{f0} > 0$ ), where turbulence is modified such that  $\delta_{hyd}$  is smaller than  $\delta$  ( $\eta < 1$ ).

For high values of  $l_g^+$ , the ratio  $\eta = \delta_{hyd}/\delta$  tends to a surface-specific constant value, which we denote as  $\eta_c$ . The corresponding values are included in table 2. The observed trend indicates that the friction behaviour of drag-increasing ridges can be described by a hydraulic reference channel height in the high-Reynolds-number regime (or high  $l_g^+$  regime), which we term the hydraulic channel height regime. Widely spaced ridges such

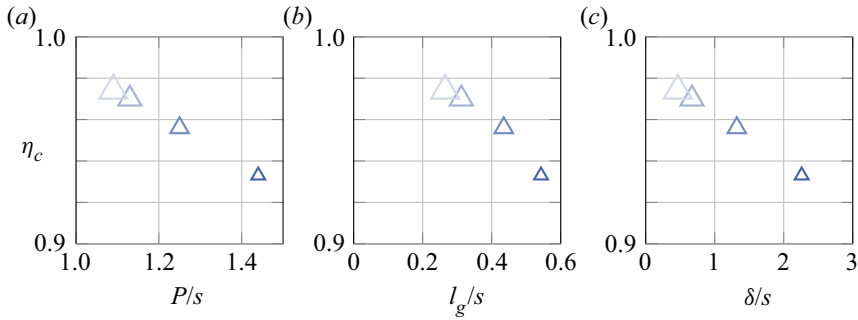


Figure 8. Constant hydraulic channel height ratio  $\eta_c$  obtained in the hydraulic channel height regime as a function of different geometrical surface properties. Larger markers indicate increasing  $s/\delta$ , with marker colours representing the individual data sets as introduced in figure 10. (a) Perimeter increase  $P/s$ ; (b)  $l_g/s$ ; (c) reciprocal spanwise wavelength  $\delta/s$ .

as di\_13 saturate to  $\eta_c$  at  $l_g^+ \approx 300$ , whereas the narrow-spaced ridges undergo a transient region and approach  $\eta_c$  at higher  $l_g^+$ : di\_2, ..., di\_8 at  $l_g^+ \approx 500$ . Given the discrepancy for the onset of the hydraulic channel height regime in terms of  $l_g^+$ ,  $l_g^+$  does not seem to be the suitable scaling to determine its onset. The existence of such a scaling remains to be investigated in future studies. We note that the observed hydraulic channel height regime is not in agreement with a constant friction increase  $\Delta C_f/C_0$  beyond the fully rough drag regime postulated by Gatti *et al.* (2020).

In order to obtain a complete predictive framework for the drag behaviour in the hydraulic channel height regime, an *a priori* definition of  $\eta_c$  would be required. The classical hydraulic diameter approach is built on the idea that geometrical parameters such as the perimeter increase  $P/s$  determine the drag behaviour. Such parameters are considered in the following, and figure 8 shows  $\eta_c$  as a function of different geometrical surface parameters, namely the relative increase of wetted surface area  $P/s$ , the square root of the groove area normalized by the tip distance  $l_g/s$ , and the reciprocal of the structure spacing normalized by the half-channel height  $\delta/s$ . The geometrical similarity of the surfaces for which we were able to achieve the hydraulic channel height regime does not allow general predictive statements, albeit that clear trends can be recognized.

Figure 8(a) reveals a nearly linearly decreasing  $\eta_c$ , and thus higher drag, with increasing  $P/s$ . For the limiting case of wide-spaced small ridges, for which the increase of wetted perimeter becomes negligibly small,  $P/s$  tends to 1. One would thus expect to retrieve  $\eta_c = 1$  at  $P/s = 1$ , which is fulfilled approximately with the observed trend in figure 8(a).

Since  $l_g$  is a length scale commonly applied to capture and unify different riblet shapes,  $l_g/s$  can be understood as a measure of groove shape versus ridge spacing. The available four data points from the present study appear to follow a nonlinear decrease  $\eta(l_g/s)$  in figure 8(b). The limit  $\eta_c = 1$  is reached in this representation for increasing  $s$  at fixed  $h$ , decreasing  $h$  at fixed  $s$ , or a combination of both. Again, this limiting data case is retrieved approximately by the observed data trend.

The constant hydraulic channel height ratio  $\eta_c$  as a function of the reciprocal spanwise wavelength  $s/\delta$  is plotted in figure 8(c) such that the limiting case of a smooth wall ( $\eta_c = 1$ ) is located at  $\delta/s = 0$ . In this representation, a linear trend is also observed, which agrees reasonably well with the limiting value for a smooth wall.

Overall, all investigated surface structure features seem equally suitable to obtain a predictive correlation for  $\eta_c$ . Additional ridge configurations of varying cross-sectional

## From drag-reducing riblets to drag-increasing ridges

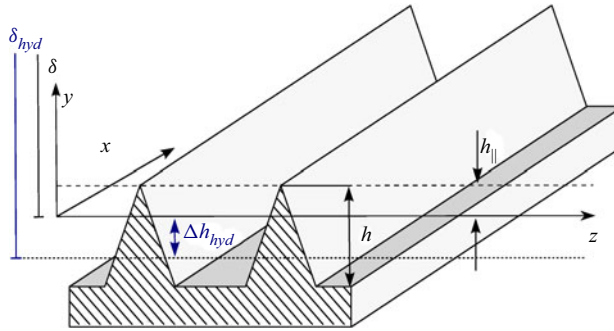


Figure 9. Sketch to illustrate the definition of the hydraulic channel height difference  $\Delta h_{hyd} = \delta_{hyd} - \delta$ . Note that  $\Delta h_{hyd}$  can assume positive and negative values depending on the drag regime.

shape need to be investigated in future studies in order to tackle a possible identification of a unified empirical or physics-informed predictive correlation for the hydraulic channel height ratio induced by ridges. This remaining challenge of an *a priori* definition for the hydraulic channel height ratio  $\eta$  can be compared to ‘the bottleneck in our ability to make full-scale predictions of drag’ (Chung *et al.* 2021) in roughness research by means of the equivalent sand grain roughness (which is also a hydraulic quantity) based on geometrical surface properties.

### 5.3.5. Hydraulic channel height difference

To further assess the change of the hydraulic channel height induced by different surface structures in the drag decreasing and drag-increasing regimes, we introduce the hydraulic channel height difference defined as

$$\Delta h_{hyd} = \delta_{hyd} - \delta, \quad (5.7)$$

which is visualized in figure 9. Here,  $\Delta h_{hyd}$  assumes positive values if  $\eta > 1$  and is otherwise negative, thus offering an alternative way to visualize changes in  $C_f$ .

Figure 10 shows  $\Delta h_{hyd}$  normalized by the structure height  $h$  as a function of  $Re_b$  for all investigated surface structures. In this normalization, all physically large ridge structures show small negative values, indicating that the reduction of the effective channel height for turbulent flow conditions is larger than  $h_{||}$ , i.e. larger than the one that would occur in a laminar flow, but still much smaller than the maximum height of the structures. In contrast, the physically smaller riblet surface structures result in values  $\Delta h_{hyd}/h$  that in modulo can be significantly larger than 1. This indicates an interesting property of riblets: the origin for  $\delta_{hyd}$  can be located below the riblet valleys in the drag-reducing regime, and above the riblet tips in the drag-increasing regime.

In figure 10, constant values of  $\Delta h_{hyd}/h$  indicate the presence of the hydraulic channel height regime discussed above. In this plot versus  $Re_b$ , it appears as if this regime is also reached for the physically largest riblet case, dr\_1c. However, the resulting visualization in figure 6 suggests that this might still be a transient behaviour. Therefore, this surface structure is not considered to have reached the hydraulic channel height regime within the  $Re_b$  range of our experimental facility. In fact, we expect a decrease of  $\Delta h_{hyd}/h$  for dr\_1c beyond the fully rough regime, resulting in values more similar to the ones observed for ridges.

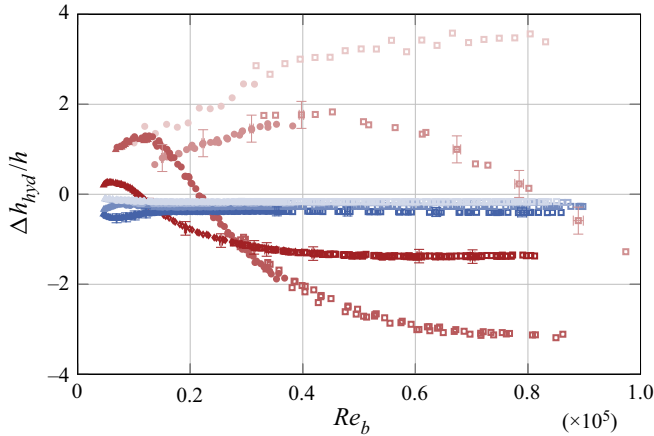


Figure 10. Hydraulic channel height difference  $\Delta h_{hyd}$  defined in analogy to the protrusion height (see sketch in figure 9 for definitions) normalized with the structure height  $h$  as a function of  $Re_b$ . Same markers as in figure 7. The horizontal and vertical error bars represent the measurement uncertainty for exemplary data points.

## 6. Concluding remarks

The high-precision pressure-drop measurements carried out on eight 2-D trapezoidal-grooved surface structures provide a comprehensive description of the occurring drag regimes spanning the well-understood drag-reducing regime, where 2-D structures are commonly termed riblets, up to the drag-increasing regime of ridge-type roughness, where such structures are usually termed ridges. Varying  $Re_b$ , the spanwise wavelength  $s$  and the structure height  $h$  over one order of magnitude allow to study the skin friction  $C_f$  and related drag change, expressed as the roughness function  $\Delta U^+$ , with respect to the smooth reference in the range  $1 < l_g^+ < 1340$ . In doing so, we investigate four 2-D surfaces with  $l_g/\delta < 0.17$  that we term riblets, and four surfaces exceeding  $l_g/\delta \approx 0.17$  that we refer to as ridges.

Investigating the drag change of three geometrically similar riblets of varying physical sizes highlights the importance of the choice of the effective channel height. In the present study, the wall-normal origin is placed at  $h_{||}$  below the crest of the 2-D structures. The streamwise protrusion height  $h_{||}$  is obtained by solving an inexpensive Poisson equation. The resulting effective channel height  $\delta$ , utilized to translate the measured pressure gradient into an equivalent wall-shear stress of a virtual flat wall, is smaller than the average channel height. The present definition ensures that the relation  $C_f = 12/Re_b$ , valid for laminar flow over flat surfaces, also holds for laminar flow above the structured ones. In this way, all surface-induced changes of  $C_f$  measured in turbulent channel flows stem from turbulent effects only. With this choice of  $\delta$ , the drag-change curves collapse remarkably well both in the drag-reducing regime (all structures achieve maximum drag reduction at  $l_g^+ \approx 11$  and cross  $\Delta C_f = 0$  at  $l_g^+ \approx 17$ ) and in the drag-increasing regime up to  $l_g^+ \approx 40$ .

The challenge of choosing a physically sound value of  $\delta$  is shared by many recent studies (Chan-Braun, Garca-Villalba & Uhlmann 2011; Endrikat *et al.* 2021; Ibrahim *et al.* 2021) involving surface structuring, not only of the 2-D kind addressed here. Even numerical studies, where  $\tau_w$  can be determined directly without resorting to (2.1), face this ambiguity as the different problem of the virtual wall placement, typically required to represent spanwise-averaged turbulence statistics. For instance, Ibrahim *et al.* (2021) propose a

virtual wall placement relying upon turbulent statistics obtained *a posteriori*. Evaluation of the effective wall-shear stress for DNS of rough wall flows (Forooghi *et al.* 2017) often also relies on *a posteriori* methods. Naturally, any *a priori* method has clear advantages for experimental studies in which the full flow field information is not available. More importantly, one has to be aware of the fact that different definitions of the effective channel height could lead to different interpretations of  $C_f$  variations, especially when the scale separation between structure size and boundary layer thickness is not very large. Since it is possible to re-evaluate  $\Delta C_f$  for different channel heights following (5.1a,b), all data published in this field should contain a clear statement about the equivalent channel height (or virtual origin) definition. Sensitivities of  $C_f$  to other equivalent channel height definitions can then be evaluated easily.

Enabled by the present choice of  $\delta$ , four main outcomes can be drawn from the analysis of the structure-induced drag changes of the present study. First, the viscous prediction of riblet drag reduction based on the difference of the streamwise ( $h_{||}$ ) and spanwise ( $h_{\perp}$ ) protrusion heights (Luchini *et al.* 1991) agrees very well with the measured drag-change curve of the physically smallest riblet set dr\_1c for  $1 < l_g^+ < 7$ . Also, for larger structures such as dr\_1c, the expected drag-reducing effect known from the literature (see, for instance, Walsh 1990; Bechert *et al.* 1997) is obtained.

Second, past the drag-reducing regime ( $l_g^+ \geq 17$ ) and up to  $l_g^+ \approx 40$ , the drag-change curves in terms of the roughness function  $\Delta U^+$  plotted against  $l_g^+$  are found to collapse onto one single curve that agrees well with the fully rough behaviour or rough wall surfaces characterized by a logarithmic increase of the roughness function  $\Delta U^+$ . Interestingly, data for geometrically similar riblets and ridges are found to collapse in this regime, confirming that the distinction between riblets and ridges is just mere nomenclature. For the equivalent sand grain roughness  $k_s$  of the identified (apparent) fully rough regime, the empirical relation  $k_s = l_g/4.4$  is found, making the drag in this regime predictable. Since riblets and ridges cannot experience any pressure drag (the dominance of which is typically associated with fully rough drag behaviour), it remains to be understood which flow phenomena induce this particular phenomenon.

Third, an unexpectedly rich drag behaviour is observed for the first time beyond the fully rough regime ( $l_g^+ \geq 40$ ). The departure from the fully rough behaviour, whose onset was already observed by Gatti *et al.* (2020) relying upon the same data set dr\_2, is confirmed distinctly here via the additional riblet geometry dr\_1c. The new data show that such deviation from the fully rough regime is very complex, with  $\Delta U^+$  exhibiting local maxima and minima for two sets of ridges, di\_2 and di\_4. Thus we term this regime, found for  $50 < l_g^+ < 200$  for the investigated geometries, the non-monotonic regime.

Finally, a drag regime beyond  $l_g^+ = 200$  is identified in which a hydraulic channel height ratio (similar to a hydraulic diameter concept) is sufficient to describe the drag behaviour of ridges. Riblets might also eventually reach such a regime, but this is not the case for the presently investigated riblet shapes within the Reynolds number range of the experimental facility. The hydraulic channel height ratio  $\eta$  is a quantity obtained *a posteriori* that compares the effective hydraulic channel height under turbulent flow conditions to its laminar counterpart, which is exactly the equivalent channel height  $\delta$  employed for the present study. In the hydraulic channel height regime,  $\eta$  assumes a constant but surface-specific value  $\eta_c$ . Relating this hydraulic surface property to geometrical surface properties remains an open task for which data for different ridge geometries are required.

**Acknowledgements.** We would like to thank P. Luchini for fruitful discussions on riblet drag reduction, in particular with respect to the physical relevance of the streamwise protrusion height in laminar and turbulent flow. We thank W. Hage for providing the 3M riblet foils that correspond to data sets dr\_1a and dr\_1b, and the Institute of Production Science (wbk) at KIT for manufacturing riblet set dr\_1c.

**Funding.** We gratefully acknowledge support through Priority Programme SPP 1881 Turbulent Superstructures of the Deutsche Forschungsgemeinschaft (DFG), project nos 316200959 and 429326502.

**Declaration of interests.** The authors report no conflict of interest.

**Data availability statement.** A database featuring all shown measurement results is in preparation and will be linked to the present publication.

**Author ORCIDs.**

 Lars H. von Deyn <https://orcid.org/0000-0003-1090-185X>;

 Davide Gatti <https://orcid.org/0000-0002-8178-9626>;

 Bettina Frohnappel <https://orcid.org/0000-0002-0594-7178>.

**Author contributions.** L.H.v.D.: investigation, data curation, formal analysis, writing (original draft), visualization, project administration. D.G.: conceptualization, methodology, formal analysis, supervision, writing (review and editing). B.F.: conceptualization, methodology, formal analysis, supervision, writing (review and editing), funding acquisition, project administration

## Appendix. Drag-change measurements scaled with alternative channel height definitions

In the present work, the parallel protrusion height  $h_{\parallel}$  is utilized to define the channel height (see § 2) in order to discern drag changes in structured channels caused by turbulence. However, a number of different channel height definitions are commonly applied in the literature. Besides a definition based on the surface meltdown height as already discussed in § 5.2 (see figure 5), other common choices include channel heights based on the spanwise protrusion height (see e.g. Ibrahim *et al.* 2021) or the structure crests (see e.g. Schönecker & Hardt 2015). In figure 11, the drag change results for riblets are re-scaled for these channel height definitions. The variables are denoted by  $(\cdot)_{\perp}$  and  $(\cdot)_{tip}$ , such that  $\delta_{tip}$  corresponds to the smallest reference channel height among all discussed choices, whereas  $\delta_{\perp}$  lies between  $\delta$  and  $\delta_{tip}$ .

In agreement with the observations with respect to figure 5, a smaller reference channel height leads to a larger relative change of  $C_f$ . This is particularly true for larger surface structures, while smaller ones (such as dr\_1a and dr\_1b, for which  $h/\delta \ll 1$ ) reveal hardly any difference. In both representations of figure 11, the set dr\_1c achieves a relative change of  $C_f$  comparable to or larger (in absolute value) than sets dr\_1a and dr\_1b. This result is unexpected, given that the shape of these sets is geometrically similar but dr\_1c has rounded riblet tips, which is known in the literature to be associated with reduced riblet performance (Walsh 1990).

It can be seen that also the zero crossing for  $\Delta C_f$  is influenced by the channel height definition. Very good collapse of all data sets at this location is obtained for both channel height definitions in figure 11, albeit at different values of  $l_g^+$ .

Overall, these different types of data evaluation indicate that the choice of reference channel height strongly influences the drag values obtained through pressure-drop evaluation of internal flow when large-scale separation between the surface structure or roughness size and the boundary layer thickness is not fulfilled. It is thus of utmost importance that the choice of the reference channel height is reported clearly for such cases. *A posteriori* translation of the results for other reference channel heights can then be carried out following (5.1a,b).

From drag-reducing riblets to drag-increasing ridges

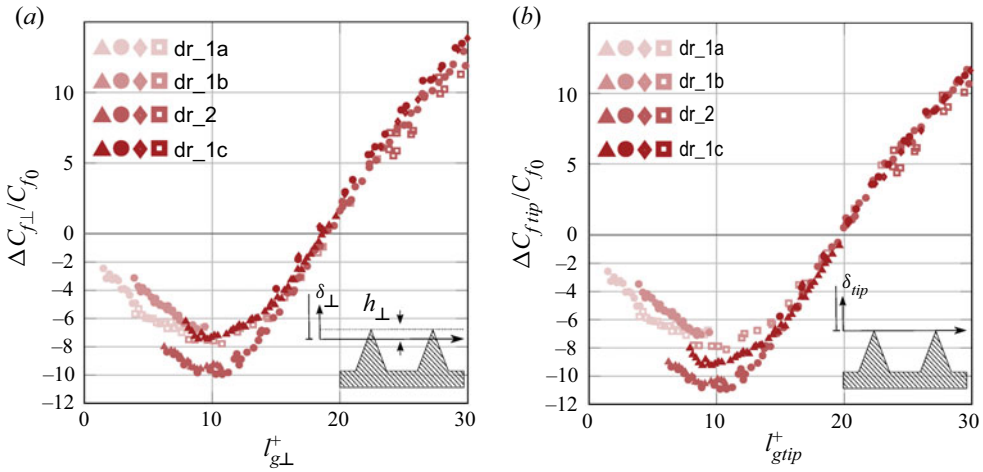


Figure 11. Effect of other wall-normal origin definitions on the drag-change curves. Same as figure 5, but different wall-normal origins: (a) wall-normal origin placed at  $h_{\perp}$  below the structure crest; (b) wall-normal origin placed at the structure tip.

REFERENCES

- BARROS, J.M. & CHRISTENSEN, K.T. 2014 Observations of turbulent secondary flows in a rough-wall boundary layer. *J. Fluid Mech.* **748**, R1.
- BARROS, J.M., SCHULTZ, M.P. & FLACK, K.A. 2018 Measurements of skin-friction of systematically generated surface roughness. *Intl J. Heat Fluid Flow* **72**, 1–7.
- BECHERT, D.W. & BARTENWERFER, M. 1989 The viscous flow on surfaces with longitudinal ribs. *J. Fluid Mech.* **206**, 105–129.
- BECHERT, D.W., BRUSE, M., HAGE, W., HOEVEN, J.G.T.V.D. & HOPPE, G. 1997 Experiments on drag-reducing surfaces and their optimization with an adjustable geometry. *J. Fluid Mech.* **338**, 59–87.
- CHAN, L., MACDONALD, M., CHUNG, D., HUTCHINS, N. & OOI, A. 2015 A systematic investigation of roughness height and wavelength in turbulent pipe flow in the transitionally rough regime. *J. Fluid Mech.* **771**, 743–777.
- CHAN-BRAUN, C., GARCÍA-A-VILLALBA, M. & UHLMANN, M. 2011 Force and torque acting on particles in a transitionally rough open-channel flow. *J. Fluid Mech.* **684**, 441–474.
- CHUNG, D., HUTCHINS, N., SCHULTZ, M.P. & FLACK, K.A. 2021 Predicting the drag of rough surfaces. *Annu. Rev. Fluid Mech.* **53**, 439–471.
- COLEBROOK, C.F., BLENCH, T., CHATLEY, H., ESSEX, E.H., FINNIEOME, J.R., LACEY, G., WILLIAMSON, J. & MACDONALD, G.G. 1939 Turbulent flow in pipes, with particular reference to the transition region between the smooth and rough pipe laws. *J. Inst. Civil Engrs* **12**, 393–422.
- COLOMBINI, M. 1993 Turbulence-driven secondary flows and formation of sand ridges. *J. Fluid Mech.* **254**, 701–719.
- DEAN, R.B. 1978 Reynolds number dependence of skin friction and other bulk flow variables in two-dimensional rectangular duct flow. *J. Fluids Engng* **100**, 215–223.
- VON DEYN, L.H., ÖRLÜ, R., GATTI, D., KRIEGSEIS, J., FROHNAPFEL, B. & STROH, A. 2019 Turbulent channel flows with secondary motions: a concerted DNS and experimental study. In *11th International Symposium on Turbulence and Shear Flow Phenomena*.
- VON DEYN, L.H., SCHMIDT, M., ÖRLÜ, R., STROH, A., KRIEGSEIS, J., BÖHM, B. & FROHNAPFEL, B. 2021 Ridge-type roughness: from turbulent channel flow to internal combustion engine. *Exp. Fluids* **63**, 18.
- ENDRIKAT, S., MODESTI, D., GARCÍA-MAYORAL, R., HUTCHINS, N. & CHUNG, D. 2021 Influence of riblet shapes on the occurrence of Kelvin–Helmholtz rollers. *J. Fluid Mech.* **913**, A37.
- FLACK, K.A., SCHULTZ, M.P. & BARROS, J.M. 2020 Skin friction measurements of systematically-varied roughness: probing the role of roughness amplitude and skewness. *Flow Turbul. Combust.* **104**, 317–329.
- FOROOGHI, P., STROH, A., MAGAGNATO, F., JAKIRLIĆ, S. & FROHNAPFEL, B. 2017 Toward a universal roughness correlation. *J. Fluids Engng* **139** (12), 121201.

- GARCÍA-MAYORAL, R., GÓMEZ-DE-SEGURA, G. & FAIRHALL, C.T. 2019 The control of near-wall turbulence through surface texturing. *Fluid Dyn. Res.* **51**, 011410.
- GARCÍA-MAYORAL, R. & JIMÉNEZ, J. 2011a Drag reduction by riblets. *Phil. Trans. R. Soc. A* **369**, 1412–1427.
- GARCÍA-MAYORAL, R. & JIMÉNEZ, J. 2011b Hydrodynamic stability and breakdown of the viscous regime over riblets. *J. Fluid Mech.* **678**, 317–347.
- GATTI, D., VON DEYN, L.H., FOROOGHI, P. & FROHNAPPFEL, B. 2020 Do riblets exhibit fully rough behaviour? *Exp. Fluids* **61**, 81.
- GATTI, D., GÜTTLER, A., FROHNAPPFEL, B. & TROPEA, C. 2015 Experimental assessment of spanwise-oscillating dielectric electroactive surfaces for turbulent drag reduction in an air channel flow. *Exp. Fluids* **56**, 110.
- GOLDSTEIN, D.B. & TUAN, T.C. 1998 Secondary flow induced by riblets. *J. Fluid Mech.* **363**, 115–151.
- GRÜNEBERGER, R. & HAGE, W. 2011 Drag characteristics of longitudinal and transverse riblets at low dimensionless spacings. *Exp. Fluids* **50**, 363–373.
- GÜTTLER, A. 2015 High accuracy determination of skin friction differences in an air channel flow based on pressure drop measurements. Doctoral Thesis, Karlsruher Institut für Technologie (KIT).
- HECHT, F. 2012 New development in FreeFem++. *J. Numer. Maths* **20** (3–4), 251–265.
- HWANG, H.G. & LEE, J.H. 2018 Secondary flows in turbulent boundary layers over longitudinal surface roughness. *Phys. Rev. Fluids* **3**, 014608.
- IBRAHIM, J.I., GÓMEZ-DE-SEGURA, G., CHUNG, D. & GARCÍA-MAYORAL, R. 2021 The smooth-wall-like behaviour of turbulence over drag-altering surfaces: a unifying virtual-origin framework. *J. Fluid. Mech* **915**, 87–109.
- INTERNATIONAL ORGANIZATION FOR STANDARDIZATION 2003a ISO 5167-1:2003 Measurement of fluid flow by means of pressure differential devices inserted in circular cross-section conduits running full – Part 1: General principles and requirements. ISO.
- INTERNATIONAL ORGANIZATION FOR STANDARDIZATION 2003b ISO 5167-2:2003 Measurement of fluid flow by means of pressure differential devices inserted in circular cross-section conduits running full – Part 2: Orifice plates. ISO.
- JIMÉNEZ, J. 2004 Turbulent flows over rough walls. *Annu. Rev. Fluid Mech.* **36**, 173–196.
- LUCHINI, P., MANZO, F. & POZZI, A. 1991 Resistance of a grooved surface to parallel flow and cross-flow. *J. Fluid Mech.* **228**, 87–109.
- MEDJNOUN, T., VANDERWEL, C. & GANAPATHISUBRAMANI, B. 2020 Effects of heterogeneous surface geometry on secondary flows in turbulent boundary layers. *J. Fluid Mech.* **886**, A31.
- MEHTA, R.D. & BRADSHAW, P. 1979 Design rules for small low speed wind tunnels. *Aeronaut. J.* **83**, 443–453.
- MODESTI, D., ENDRIKAT, S., HUTCHINS, N. & CHUNG, D. 2021 Dispersive stresses in turbulent flow over riblets. *J. Fluid Mech.* **917**, A55.
- PERRY, A.E., SCHOFIELD, W.H. & JOUBERT, P.N. 1969 Rough wall turbulent boundary layers. *J. Fluid Mech.* **37**, 383–413.
- PIROZZOLI, S. 2018 On turbulent friction in straight ducts with complex cross-section: the wall law and the hydraulic diameter. *J. Fluid Mech.* **846**, R1.
- SATTARY, J.A. & READER-HARRIS, M.J. 1996 The orifice plate discharge coefficient equation for iso 5167-1. In *Proceedings of the 14th North Sea Flow Measurement Workshop*, pp. 25–28.
- SCHILLER, L. 1923 Über den Strömungswiderstand von Röhren verschiedenen Querschnitts und Rauigkeitsgrades. *Z. Angew. Math. Mech.* **3**, 2–13.
- SCHÖNECKER, C. & HARDT, S. 2015 Assessment of drag reduction at slippery, topographically structured surfaces. *Microfluid. Nanofluid.* **19** (1), 199–207.
- STROH, A., SCHÄFER, K., FOROOGHI, P. & FROHNAPPFEL, B. 2020 Secondary flow and heat transfer in turbulent flow over streamwise ridges. *Intl J. Heat Fluid Flow* **81**, 108518.
- WALSH, M.J. 1990 Effect of detailed surface geometry on riblet drag reduction performance. *J. Aircraft* **27**, 572–573.
- WALSH, M.J. & LINDEMANN, A.M. 1984 Optimization and application of riblets for turbulent drag reduction. In *22nd Aerospace Sciences Meeting. AIAA Paper* 1984-347.